Journal of
Marine Science and Engineering

MDPI

Article

Integrating Computational Fluid Dynamics for Maneuverability Prediction in Dual Full Rotary Propulsion Ships: A 4-DOF Mathematical Model Approach

Qiaochan Yu [1,2], Yuan Yang [3], Xiongfei Geng [1], Yuhan Jiang [4], Yabin Li [5] and Yougang Tang [3,*]

[1] China Waterborne Transport Research Institute, Beijing 100088, China; yuqiaochan@wti.ac.cn (Q.Y.)
[2] School of Electrical and Information Engineering, Tianjin University, Tianjin 300072, China
[3] School of Civil Engineering, Tianjin University, Tianjin 300354, China
[4] Intelligent Navigation (Qingdao) Technology Co., Ltd., Qingdao 266200, China
[5] Qingdao Institute of Shipping Development Innovation, Qingdao 266200, China
* Correspondence: tangyougang_td@163.com

Abstract: To predict the maneuverability of a dual full rotary propulsion ship quickly and accurately, the integrated computational fluid dynamics (CFD) and mathematical model approach is performed to simulate the ship turning and zigzag tests, which are then compared and validated against a full-scale trial carried out under actual sea conditions. Initially, the RANS equations are solved, employing the Volume of Fluid (VOF) method to capture the free water surface, while a numerical simulation of the captive model test is conducted using the rigid body motion module. Secondly, hydrodynamic derivatives for the MMG model are obtained from the CFD simulations and empirical formula. Lastly, a four-degree-of-freedom mathematical model group (MMG) maneuvering model is proposed for the dual full rotary propulsion ship, incorporating full-scale simulations of turning and zigzag tests followed by a full-scale trial for comparative validation. The results indicate that the proposed method has a high accuracy in predicting the maneuverability of dual full-rotary propulsion ships, with an average error of less than 10% from the full-scale trial data (and within 5% for the tactical diameters in particular) in spite of the influence of environmental factors such as wind and waves. It provides experience in predicting the maneuverability of a full-scale ship during the ship design stage.

Keywords: ship maneuvering; CFD; fully rotary propulsion; MMG mathematical model; full-scale trial

Citation: Yu, Q.; Yang, Y.; Geng, X.; Jiang, Y.; Li, Y.; Tang, Y. Integrating Computational Fluid Dynamics for Maneuverability Prediction in Dual Full Rotary Propulsion Ships: A 4-DOF Mathematical Model Approach. *J. Mar. Sci. Eng.* **2024**, *12*, 762. https://doi.org/10.3390/jmse12050762

Academic Editor: María Isabel Lamas Galdo

Received: 29 March 2024
Revised: 26 April 2024
Accepted: 29 April 2024
Published: 30 April 2024

1. Introduction

Ship maneuverability, a pivotal aspect of maritime performance research, is essential for the assurance of navigational safety. Methods for predicting ship maneuvering performance are categorized into three principal types [1]: no simulation, system-based simulation and computational fluid dynamics (CFD)-based simulation. No simulation methods encompass database approaches, full-scale trials and free-running model tests. The former primarily utilizes regression analysis for swift evaluation, while the latter employs targeted experiments to directly ascertain maneuverability performance. The system-based simulation approach integrates hydrodynamic coefficients with equations of motion for ship maneuverability, facilitating the calculation of the ship's trajectory and associated motion parameters to predict its maneuverability.

Broadly, the assessment of ship maneuverability favors methods that are straightforward, efficient and cost-effective. These include approaches grounded in regression formulas based on characteristic parameters, database methods, free-running model test and numerical analyses employing mathematical models [2]. Mathematical models for ship maneuvering are principally divided into response models and hydrodynamic models. Response models establish a direct link between the ship's state of motion and rudder actions via navigational tests, enabling the analysis and resolution of maneuvering characteristics. Regarding hydrodynamic models, two primary mathematical models are predominantly utilized. (See Figure 1).

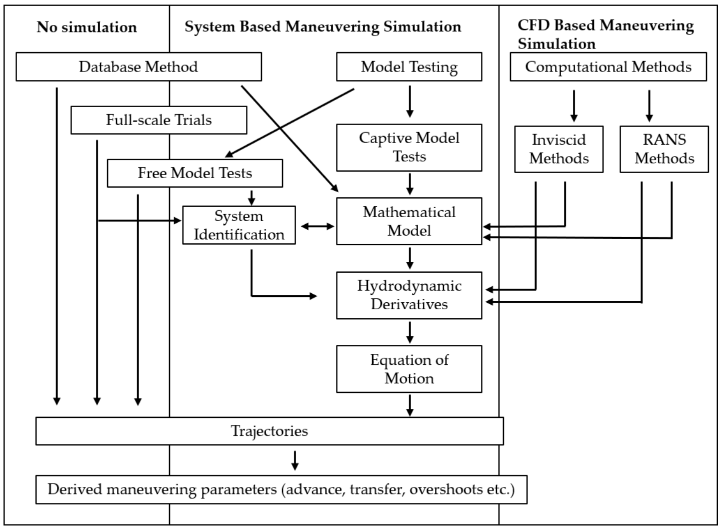

Figure 1. Maneuvering prediction methods [1].

The first model is the integrated structure model delineated by Abkowitz [3], which examines the hull, propeller and rudder collectively along with the cumulative force exerted. The second model, the Ship Maneuvering Mathematical Model Group (MMG model [4]), introduced by the Japanese Towing Tank Committee (JTTC), conducts separate hydrodynamic calculations for the hull, propeller and rudder, taking into account their interferences. Meng et al. [5] developed a response mathematical model for the vessel YUKUN, integrating Support Vector Regression with a modified grey wolf optimizer to obtain reference values for the model's parameters. Fossen [6] performed the theory and practice research on nonlinear ship control in response to the mathematical model. Svilicic et al. [7] assessed collision risks for the KVLCC2 ship through accurate modelling of ship maneuverability using non-linear FEM (NFEM). The Abkowitz maneuvering model is implemented in the LS-Dyna software code and is therefore coupled with FEM calculations. Shin et al. [8] investigated the maneuverability of a KCS equipped with energy-saving devices utilizing the MMG model. Reichel [9] introduced a novel characterization of forces on azimuth thrusters within the motion mathematical model, employing MMG methodology and experimentally validating its accuracy.

Both methods necessitate precise hydrodynamic derivative calculations to develop an accurate model of ship maneuverability. The extensive application of CFD techniques facilitates more precise outcomes in ship hydrodynamics analysis, design and maneuverability forecasting. Given this backdrop, numerous researchers have advanced static and dynamic simulations to study ship maneuvering movements. Sun et al. [10] utilized the STAR-CCM+ software to model the Planar Motion Mechanism (PMM) of the hull through the overlapping grid technique, deriving hydrodynamic derivatives subsequently integrated into the MMG model for twin waterjet propulsion vessels. Ahmad et al. [11] performed Oblique Towing Tests (OTT) and dynamic Planar Motion Mechanism (PMM) analyses on the vessel DTMB 5512 using CFD simulations to determine the hydrodynamic derivatives.

In ship maneuverability modeling, the four-Degree-of-Freedom (4-DOF) MMG model is broadly embraced for its clear-cut derivatives and efficient computation, particularly emphasizing the impact of ship roll. R. Rajita et al. [12] addressed the calculation of linear, nonlinear and roll-coupled hydrodynamic derivatives for a container ship through CFD-based numerical simulations of static and dynamic tests across various roll angles. Li et al. [13] executed Oblique Towing Tests (OTT) and dynamic Circular Motion Tests (CMT) to collect essential data for MMG model identification, and they simulated the free-running maneuverability test using a body force propeller approach that obviates the need for detailed flow field construction around the propeller. Guo et al. [14] investigated the 4-DOF ship maneuvering motion in calm water for the ONR tumblehome model by a system-based method. The result indicates the validity of the CFD-based modelling method for the hull−propeller−rudder interaction of twin-screw ships. Okuda et al. [15] applied the 4-DOF MMG method as a practical simulation method that includes the roll-coupling effect to predict the maneuvering of a KCS at fast speeds. Dash et al. [16] developed a 4-DOF simulation method for the maneuvering motion of a ship with a twin propeller and twin rudder system. The hydrodynamic derivatives and parameters were determined by the PMM tests, and roll-induced bifurcation in maneuvering was discussed by the simulations.

Likewise, the discretized propeller approach can simulate free-running maneuverability tests. Shen et al. [17] implement the dynamic overset grid technique into naoe-FOAM-SJTU solver to simulate standard 10/10 zig-zag maneuver and modified 15/1 zig-zag maneuver of KCS, which showed good agreement with the experiment data. Wang et al. [18] studied the free running test of the ONR Tumblehome ship model under course keeping control with twin actual rotating propellers and moving rudders, and a new course keeping control module was developed using a feedback controller based on the CFD solver. Carrica et al. [19] conducted a study on a KCS container ship performing a zigzag maneuver in shallow water experimentally and numerically using direct discretization of a moving rudder and propeller. The zigzag maneuver at the nominal rudder rate uses grids of up to 71.3 million points. Sanada et al. [20] performed research on the hull–propeller–rudder interaction at the Korea Research Institute of Ships using a combined experimental fluid dynamic and CFD method, with an innovative approach being employed for the analysis of steady state circular motions. Nonetheless, both techniques demand significant computational resources and time costs to precisely model ship maneuvering movements, especially for a full rotary ship. Consequently, integrating mathematical modeling with CFD simulations of captive model tests has proven to enhance forecasting speed while maintaining a balance between rapidity and accuracy [21].

Full rotary propellers, as opposed to conventional rudder and propeller setups, possess enhanced maneuvering capabilities, adeptly dealing with intricate scenarios like stationary rotation and sideways motion [22]. It is shown that a ship's stability can be jeopardized in terms of excessive heeling in calm water or parametric rolling in extreme waves due to low GM and damping characteristics. The effect of GM or loading conditions due to the accommodation of full rotary propellers have been more apparent between runs in design draught and scantling draught conditions [23]. Currently, limited calculations and simulations fully account for the impact of dual full rotary propellers on ship maneuverability, with reliance primarily being on free-running tests or full-scale trials. Neatby et al. [24] performed comprehensive full-scale trials, encompassing turning circles, effective turning tests and crash stops, on a vessel equipped with dual Z-drive thrusters. Reichel [9] introduced a 3-DOF mathematical model grounded in MMG methodology, conducting both numerical simulations and experimental validations on a pod-driven coastal tanker. This approach verified the model's capability to discern performance trends, even in vessels with unstable trajectories. Piaggio et al. [25] showcased the findings of a comparative analysis between spade and flap rudder configurations versus pod-driven systems for a select fleet, demonstrating that appropriately designed pod units do not compromise yaw control capabilities.

Conducting full rotary propulsion ship free-running tests via direct CFD simulations necessitates a finer grid mesh, thereby increasing the demand for computational resources and extending the time required for analysis. Meanwhile, the current research on the maneuverability of dual full-rotary propulsion ships lacks consideration of rolling conditions, and the high DOF motion of the propeller makes direct CFD simulation more difficult. Viewed comprehensively, research on fast motion prediction of dual full-rotary propulsion ships is still relatively scant, and related theoretical studies and practical problems still need to be examined.

This paper introduces a fast-time prediction technique for predicting ship maneuverability. Utilizing CFD methods, this study simulates the captive model test of the "Zhifei" [26] ship to derive its hydrodynamic derivatives. Furthermore, it presents a 4-DOF MMG mathematical model for dual full rotary propulsion ships. Numerical simulations on full-scale tests were performed on the "Zhifei" ship for turning and zigzag maneuvers in calm waters, with the results being compared against experimental full-scale trial data to confirm the viability of the proposed maneuvering model for dual full-rotary propulsion ships. This approach offers a reliable solution for the precise prediction of maneuverability during the ship's design stage.

2. Mathematical Model and Method

2.1. Coordinate and MMG Model

The development of mathematical models for maneuvering motions necessitates establishing earth-fixed and ship-fixed coordinate systems to delineate the pertinent motion variables. Within the earth-fixed coordinate framework, ship movement is characterized by the spatial coordinates $[x, y, z]^{\mathrm{T}}$ and the orientation angles $[\varphi, \theta, \psi]^{\mathrm{T}}$. $O_0 - X_0Y_0Z_0$ is fixed to a specific point on the earth's surface, with the Z_0 axis being oriented vertically downwards. $G - xyz$ is attached to the ship's center of gravity, with the x axis being directed towards the bow and the y axis towards the starboard side, while the z axis extends vertically downwards. Generally, analyzing such problems requires facilitating the mutual conversion between these two coordinate systems, which are shown in Figure 2.

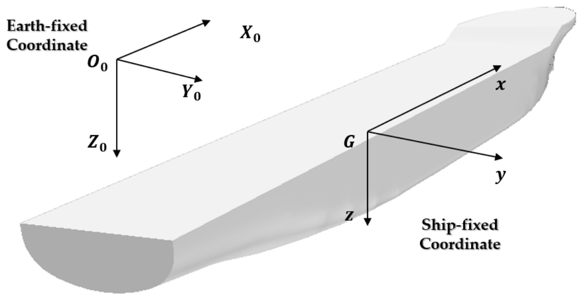

Figure 2. Coordinate systems.

Following the concept of segregated ship-motion mathematical modeling, the array of forces and moments exerted on the ship is categorically allocated to the bare hull and the propeller for computational purposes. The four-degree-of-freedom motion equations for a dual full rotary propelled ship within the designated coordinate system are derived, accounting for the ship's rolling state, as follows [14]:

$$\begin{aligned} (m+m_x)\dot{u} - (m+m_y)vr &= X_{\mathrm{H}} + X_{\mathrm{P}} \\ (m+m_y)\dot{v} + (m+m_x)ur &= Y_{\mathrm{H}} + Y_{\mathrm{P}} \\ (I_{xx}+J_{xx})\dot{p} &= K_{\mathrm{H}} + K_{\mathrm{P}} \\ (I_{zz}+J_{zz})\dot{r} &= N_{\mathrm{H}} + N_{\mathrm{P}} \end{aligned} \tag{1}$$

where X_{P}, Y_{P}, K_{P} and N_{P} are the longitudinal thrust force, lateral thrust force, rolling moment and yawing moment acted on the ship by the full rotary propeller, respectively, while X_{H}, Y_{H}, K_{H} and N_{H} are the hydrodynamic forces (moments) acting on different degrees of freedom of the hull by all other external forces except the propellers. Additionally, m is the mass of the ship and m_x and m_y are the additional mass of the ship in the x axis and y axis, respectively. It is caused by the co-motion of the water around the hull of the ship. I_{zz} and J_{zz} are the inertia of the ship around the z axis and the additional inertia, respectively.

2.2. Hull Hydrodynamic and Propeller Thrust Model

The hydrodynamic forces can be divided into two categories according to their causes: one is fluid inertial forces and the other is fluid viscous forces. On the basis of the Kijimas research [27], a model for estimating the hydrodynamic forces of the hull is summarized based on the consideration of the rolling moment caused by the ship's motion:

$$\begin{aligned}
&X_{\mathrm{H}} = X(u) + X_{vv}v^2 + X_{vr}vr + X_{rr}r^2 \\
&Y_{\mathrm{H}} = Y_v v + Y_r r + Y_{v|v|}v|v| + Y_{r|r|}r|r| + Y_{vvr}v^2 r + Y_{vrr}vr^2 + Y_{\mathrm{H1}}(v, r, \varphi) \\
&K_{\mathrm{H}} = -K_1(\dot{\varphi}) - K_2(\varphi) - Y_{\mathrm{H}}z_H \\
&N_{\mathrm{H}} = N_v v + N_r r + N_{v|v|}v|v| + N_{r|r|}r|r| + N_{vvr}v^2 r + N_{vrr}vr^2 + N_{\mathrm{H1}}(v, r, \varphi)
\end{aligned} \tag{2}$$

where $X(u)$ is the ship resistance when sailing straight, $K_1(\dot{\varphi})$ is the rolling damping moment, $K_2(\varphi)$ is the rolling restoring moment, $Y_{\mathrm{H}}z_H$ is the rolling moment of the hull hydrodynamic force Y_{H} on the x axis, while z_H is the z axis coordinate of the point where Y_{H} acts.

This study focuses on a ship equipped with dual full rotary propeller propulsion, as illustrated in Figure 3. The propellers are symmetrically positioned, with a longitudinal distance of L_{op} from the ship's center of gravity and a lateral separation of L_{ps} between them.

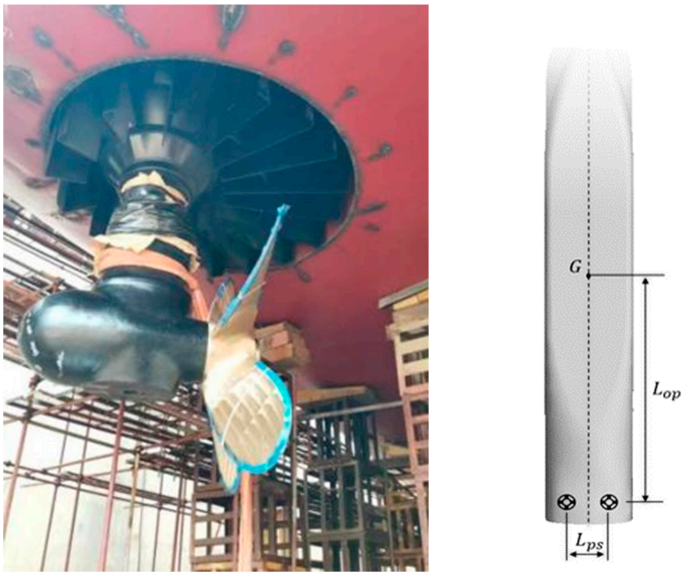

(**a**) (**b**)

Figure 3. Schematic. (**a**) Full Rotary Propeller of Ship "ZhiFei". (**b**) Propellers Position.

In the propulsion system of ships with full rotary twin-propellers, both forward movement and steering capabilities are achieved by manipulating the propellers' orientation or exploiting the differential in their rotational speeds. This technique allows for the generation of axial thrust by the propellers in static water, as follows [28]:

$$\begin{aligned}
T_p &= (1 - t_p)\rho n_p^2 D^4 k_{T(p)} \\
T_s &= (1 - t_p)\rho n_s^2 D^4 k_{T(s)}
\end{aligned} \tag{3}$$

where t_p is the thrust deduction coefficient, the subscript p and s represent the portside and starboard propellers, respectively, ρ is the density of seawater, D is the diameter of the propeller disk, n_p and n_s are the rotation speed of the left and right propellers, respectively, $k_{T(p)}$ and $k_{T(s)}$ are the coefficients of the left and right propeller thrusts open water characteristic, respectively, and calculated as follows:

$$K_T = a_0 + a_1 J + a_2 J^2 \tag{4}$$

where a_0, a_1 and a_2 are the propeller coefficients, J is the propeller advanced ratio, which is calculated as $J = u(1 - w_p)/nD$, where w_p is the wake fraction at propeller position.

When the left and right propellers work simultaneously at rotation angles δ_p and δ_s, respectively, the resulting axial thrust can be decomposed along the attached coordinate system GX and GY. Based on previous studies, we proposed the following calculation method for dual full rotary propulsion ships:

$$\begin{aligned} X_{\mathrm{P}} &= \left(T_p \cos\delta_p + T_s \cos\delta_s\right) \\ Y_{\mathrm{P}} &= \left(T_p \sin\delta_p + T_s \sin\delta_s\right) \\ K_{\mathrm{P}} &= -\cos\varphi\left(T_p \sin\delta_p + T_s \sin\delta_s\right)z_P + \tfrac{1}{2}\sin\varphi\left(T_p \sin\delta_p - T_s \sin\delta_s\right)L_{ps} \\ N_{\mathrm{P}} &= \tfrac{1}{2}\left(T_p \cos\delta_p - T_s \cos\delta_s\right)L_{ps} - Y_{\mathrm{P}} L_{op} \end{aligned} \tag{5}$$

where z_P is the distance of the horizontal center axis of propeller and the center of gravity.

2.3. Governing Equations

This study employs a CFD method to simulate the hydrodynamic forces acting on a ship. The viscous flow is approximated using the Reynolds-averaged Navier–Stokes (RANS) equations. This approach converts a transient problem into a steady-state problem by averaging over time the random fluctuation terms in the viscous flow, thereby facilitating problem resolution. The continuity equation applicable to viscous flow is presented as follows:

$$\frac{\partial(u_i)}{\partial x_i} = 0 \tag{6}$$

The Reynolds-averaged Navier–Stokes equation is:

$$\rho\frac{\partial u_i}{\partial t} + \rho u_j \frac{\partial u_i}{x_j} = -\frac{\partial \boldsymbol{P}}{\partial x_i} + \frac{\partial}{\partial x_j}\left(\mu\frac{\partial u_i}{\partial x_j} - \rho\overline{u_i' u_j'}\right) \tag{7}$$

where $\mu_{i,j}(i,j = 1,2,3)$ are the mean velocity vectors, $\boldsymbol{P}$ is the time-averaged value of pressure, $\rho\overline{u_i' u_j'}$ is the Reynolds stress, while u_i and u_j are the time-averaged values of the velocity component.

2.4. Full-Scale Test

As shown in Figure 4, a full-scale ship maneuverability test was conducted for the "Zhifei" in the China Nǚdao sea area under the conditions of a northeast wind of level 3–4 and sea state 3, with an average draft of 3.317 m. The test concluded with the ship's 10° turning motion, ±10° zigzag motion and ship resistance test when sailing straight. Motion data was collected using the SPS351 DGPS receiver, with a maximum dynamic error not exceeding 5 m.

Figure 4. Full-scale ship maneuverability test.

The database controlled ship−shore data synchronization based on the network status, where the ship-side network could establish a connection with the shore-side and the line status could support data communication. Typically, the signal data was stored during the experiment and uniformly transferred to the ground control PC at the shore terminal at the end of each day's experiment. The signal sampling frequency was 1 Hz.

3. Numerical Simulation of Captive Model Test

3.1. Computational Settings and Convergence Analysis

This study focuses on the "Zhifei" 300TEU smart container ship, China's inaugural coastal intelligent navigation container ship. The principal parameters concerning its hull, propeller and the numerical computations for the scaled model are detailed in Table 1. To derive the hydrodynamic derivatives of the hull, the OTT and CMT are simulated by using the RANS solver platform STAR-CCM+ (CD-adapco Company, German)with the specific calculation conditions outlined in Table 2.

Table 1. Main parameters of hull and propeller.

Name	Symbol	Unit	Ship	Model
Scale factor	λ		1	28.5
Length overall	L_{oa}	m	117.15	4.111
Length between perpendiculars	L_{pp}	m	111.3	3.905
Breadth	B	m	17.32	0.607
Draft	d	m	4.8	0.158
Displacement	Δ	m^3	4800	0.207
Block coefficient	C_b		0.7797	0.7797
Metacentric height	GM	m	5.1	0.179
Vertical center of gravity (from keel)	KG	m	6.16	0.216
Propeller diameter	D	m	2.7	0.947
Wake fraction at propeller position	ω_p		0.183	0.183
Number of blades	Z		4	4

Table 2. Computational case conditions.

Test	Fr	β(degree)	r'
Oblique Tow Test (OTT)	0.226	$\pm 11, \pm 9, \pm 6, \pm 2, 0$	0
Circular Motion Test (CMT)	0.226	0	$\pm 0.2, \pm 0.4, \pm 0.6$
Circular Motion Test (CMT)	0.226	$\pm 11, \pm 9, \pm 6, \pm 2$	$-0.2, -0.4, -0.6$

The computational region is defined as a cuboid, as depicted in Figure 5. The inlet, sides, top and bottom of the flow field domain are set as velocity inlet, and the outlet is set as pressure outlet. The hull surface is defined as no-slip walls to model the interface accurately. The dimensional size of the flow field domain is $-4L_{pp} < x < 2L_{pp}$, $-2.5L_{pp} < y < 2.5L_{pp}$, $-2.5L_{pp} < z < 1.0L_{pp}$. The velocity field function is used to simulate the velocity of each boundary. The simulation region is discretized using a trimmed mesher approach. Mesh refinement is applied to regions surrounding the hull and the free water surface to precisely capture the flow dynamics during the vessel's movement. Additionally, mesh refinement is employed at the bow and stern to enhance the resolution of the flow field captured. In the boundary layer, a four-layer prism is employed to maintain y+ around 30 for the majority of the region. The k-ε turbulence model is selected and integrated with the two-layer all y+ Wall Treatment to accurately represent the free water surface via the volume of the fluid method. Additionally, the dynamic fluid−body interaction (DFBI) module is utilized to numerically simulate the captive movement of the ship model. The computational region comprises approximately 2.55×10^6 grids in total. The grid count varies slightly under different operating conditions, with the hull surface and the grids of the computational domain being partitioned, as illustrated in Figure 6.

The convergence analysis for longitudinal forces on the hull under the condition of Fr = 0.226 was conducted during the direct flight test of the ship model, employing the methodology advocated by the International Towing Tank Conference. The mesh size and time step were scaled by a constant factor of $\sqrt{2}$. The stability of the calculation results is judged by the convergence parameter R_G, which is defined below [29]. These three cases show monotonically converge consistently and satisfy the computational requirements when $0 < R_G < 1$. (See Table 3).

$$R_G = \frac{S_2 - S_1}{S_3 - S_2} \tag{8}$$

where: S_1, S_2, S_3 are calculated results for fine, moderate and rough levels, respectively.

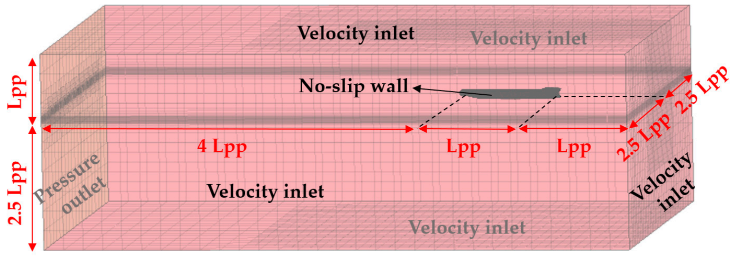

Figure 5. Computational region of captive model tests.

(**a**)

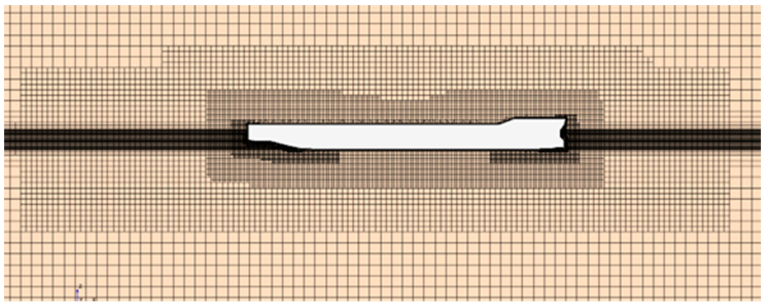

(**b**)

Figure 6. The grids in computational region: (**a**) Hull surface; (**b**) Computational region.

Table 3. Convergence analysis of mesh sizes and time steps.

Case	Name	Value	Solution Time [1]	Longitudinal Resistance	R_G
G_1		0.05 (m)	49,800 (s)	12.1556 (N)	
G_2	Mesh Size [2]	0.07 (m)	14,065 (s)	12.2694 (N)	0.341
G_3		0.10 (m)	8665 (s)	12.6028 (N)	
T_1		0.007 (s)	30,343 (s)	12.2495 (N)	
T_2	Time Step	0.010 (s)	14,065 (s)	12.2694 (N)	0.279
T_3		0.014 (s)	9586 (s)	12.3405 (N)	

[1] Time required to simulate 45 s in solver. [2] Mesh size G_1, G_2, G_3 contains the total number of grids 5.22×10^6, 2.55×10^6, 1.26×10^6, respectively.

The findings indicate that both grid size and time step exhibit convergence. Diminishing either the grid size or the time step further minimizes the errors in the computational outcomes while leading to a significant increase in the solution time. Upon verifying the precision of the calculations and considering time efficiency, the simulation method using a medium grid size G_2 and a medium time step T_2 was chosen in this study.

3.2. Resistance Validation of Straight Sailing

Conducting a numerical simulation of the resistance during straight sailing allows for additional validation of the numerical model's calculation accuracy. Furthermore, fitting the resistance function of the ship model at varying speeds enables the derivation of X(u). The specific calculation scenarios and their outcomes are detailed in Table 4. A comparison of the modeled ship's resistance with actual ship test values, post-Froude-resistance transformation, reveals an error margin of approximately 5%, with a consistent overall trend being observed. The error is within an acceptable range, taking into account factors such as scale effects and experimental error. Figure 7 illustrates the free surface wave patterns at various speeds, accurately depicting the symmetrical Kelvin waves generated by the bow and stern. The clarity of peak and trough contours further signifies the simulation's effectiveness.

Table 4. Comparison of calculation conditions and results of direct flight resistance.

$Fr = U/\sqrt{gL}$	U (m/s)	Numerical Modelled Values (N)	Froude Transform Value (N)	Test Value (N)	Error (%)
0.129	0.8	3.934	73,298.84	76,159.31	3.76
0.178	1.1	7.625	125,651.22	135,501.75	7.27
0.226	1.4	12.269	242,683.36	250,553.62	3.14
0.275	1.7	19.853	396,594.89	421,314.91	5.87
0.323	2	40.871	695,527.64	647,785.64	7.37

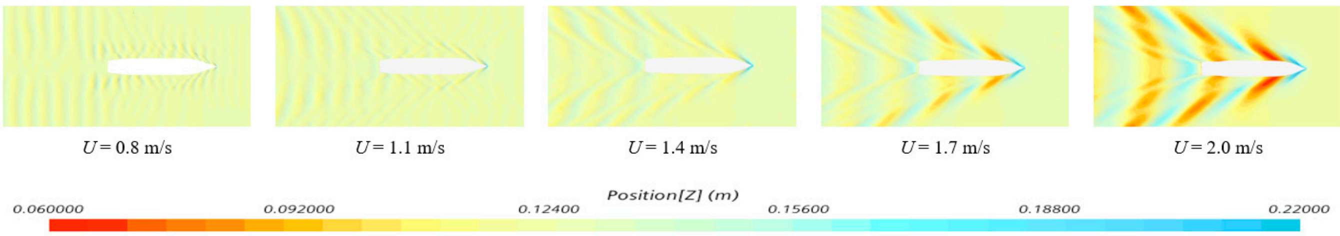

Figure 7. Free surface wave patterns at various speeds.

The calculated resistance values in the table are plotted as resistance curves, as shown in Figure 8, and the resistance function of the ship "Zhifei" is fitted as $X(u) = 420666.76u^2 - 672733.19u + 348350.78$.

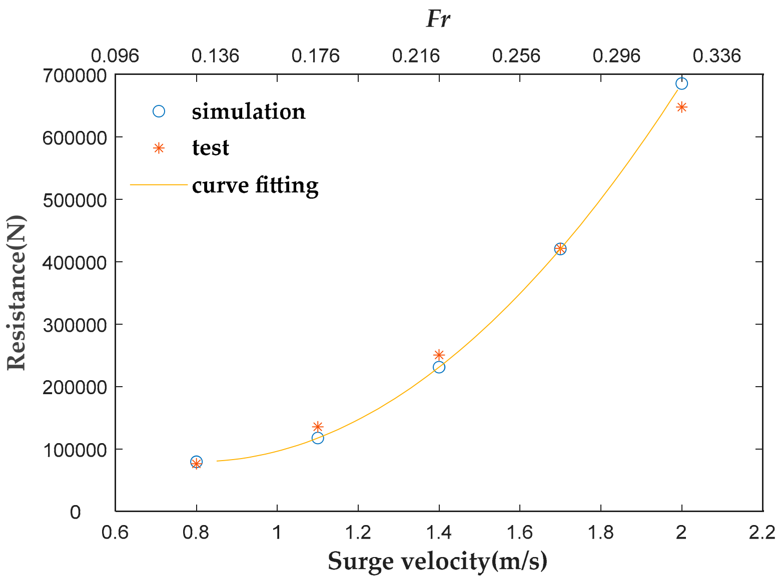

Figure 8. Resistance value and fitted curve.

3.3. Captive Model Test Simulation

The free surface wave patterns under varying test conditions are shown as follows: Figure 9 shows the simulation result of wave pattern in an oblique towing test at $\beta = 0°$, $2°$, $9°$. When $\beta = 0°$, symmetrical kelvin waves are formed at the bow and stern of the ship, and the height of the rising waves on both sides is basically identical. In contrast, as β increases, asymmetrical waves emerge on either side of the hull, becoming more pronounced. The waves at the bow and stern on the windward side converge, whereas those on the leeward side diverge, which becomes more apparent as β increases.

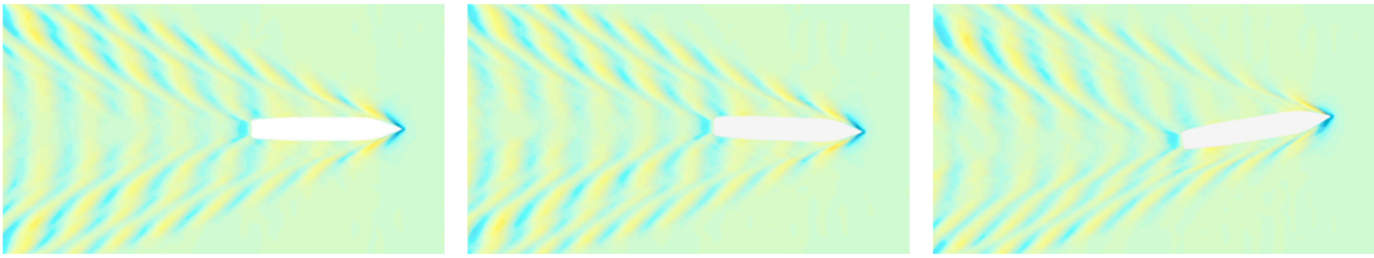

(**a**) (**b**) (**c**)

Figure 9. Wave pattern in OTT test: (**a**) $\beta = 0^{\circ}$; (**b**) $\beta = -2^{\circ}$; (**c**) $\beta = 9^{\circ}$.

Figures 10–12 depicts the circular motion test simulation with $\beta = 0°$, $-2°$, $9°$. In Figure 10, with $\beta = 0°$, the waves generated at the bow and stern of the ship continuously intersect behind the ship while sailing. The bow wave crest progressively moved towards the port side as the rate of turn r' increased, while the stern wave also curves towards the port side in response to the ship's movement. Meanwhile, the intersection becomes more obvious, and the wave area on both sides of the ship is more compact and shifted to the port side.

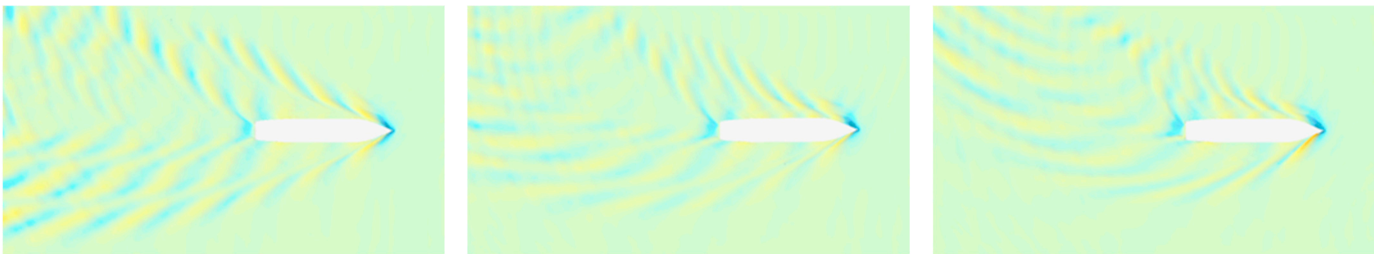

(**a**) (**b**) (**c**)

Figure 10. Wave pattern in CMT test with $\beta = 0°$: (**a**) $r' = -0.2$; (**b**) $r' = -0.4$; (**c**) $r' = -0.6$.

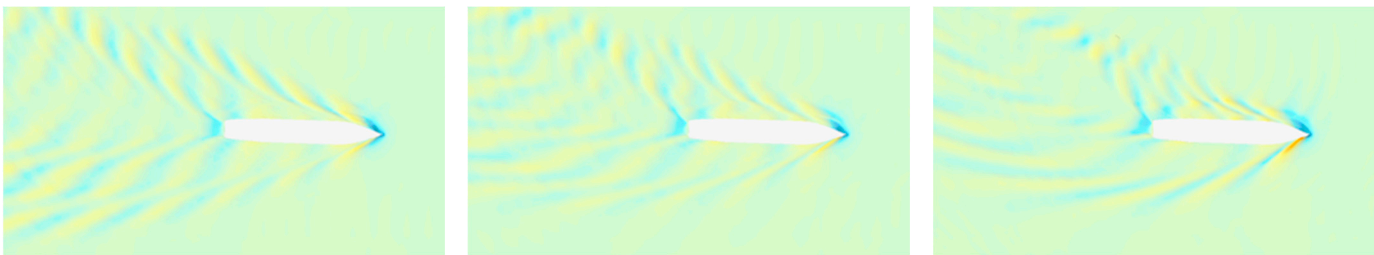

(**a**) (**b**) (**c**)

Figure 11. Wave pattern in CMT test with $\beta = -2°$: (**a**) $r' = -0.2$; (**b**) $r' = -0.4$; (**c**) $r' = -0.6$.

In Figure 11, with $\beta < 0°$, the wave amplitude along the hull significantly increases, with the predominant wave distribution shifting to the starboard side, indicating that the bow and stern waves gradually converge from the port side towards and spread to the starboard side. Meanwhile, comparing with the same r', the height of the bow rising wave increases obviously. With $\beta > 0°$, the amplitude of the waves along the hull is reduced, and the primary area of wave distribution for both bow and stern is on the port side, as shown in Figure 12.

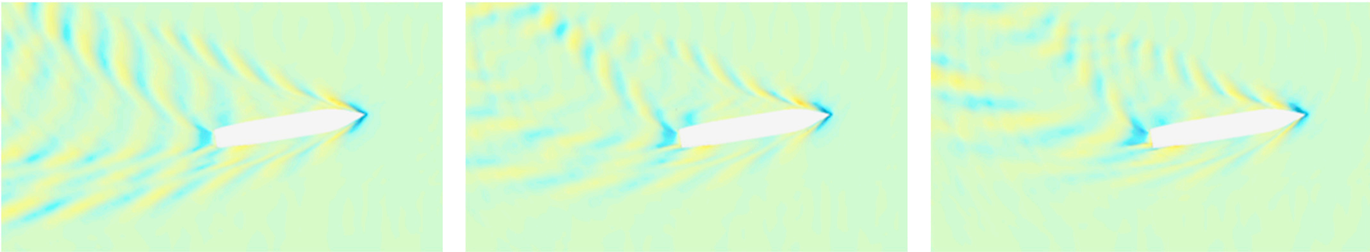

(**a**) (**b**) (**c**)

Figure 12. Wave pattern in CMT test with $\beta = 9^{\circ}$: (**a**) $r' = -0.2$; (**b**) $r' = -0.4$; (**c**) $r' = -0.6$.

Figure 13 illustrates how the waterline at the bow changes with the drift angle, highlighting that the drift angle induces an asymmetric wave pattern on both sides of the bow. This asymmetry becomes increasingly pronounced with larger drift angles.

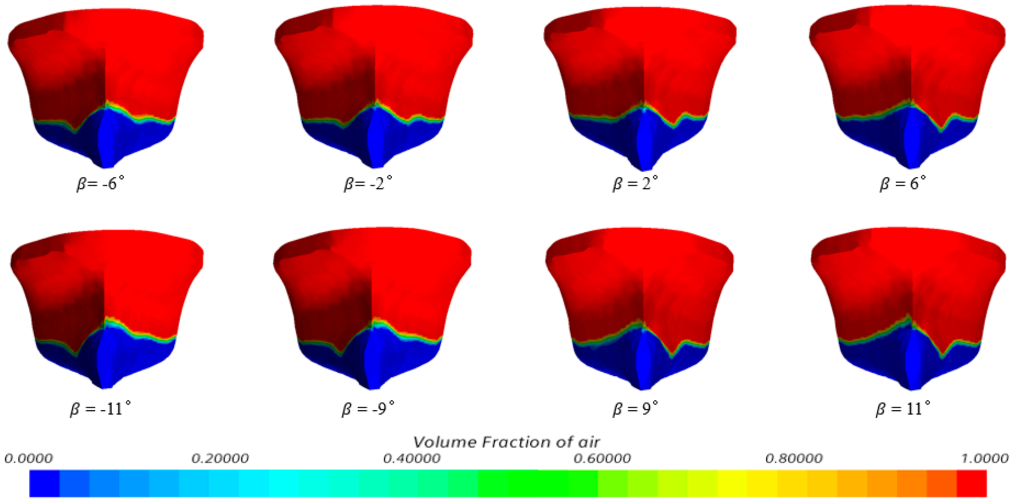

Figure 13. Bow waterline at different drift angles.

Figure 14 depicts the distribution of the pressure coefficient along the hull's bottom, providing insights into the hydrodynamic pressures exerted on the ship's underbody during various test conditions. With increasing turn rate r', the pressure on the starboard side of the ship intensifies. At a drift angle of $\beta < 0^{\circ}$, the pressure concentration at the starboard side of the bow escalates, expanding the high-pressure zone as r' rises, with a continuous increase in pressure amplitude. Conversely, at $\beta > 0^{\circ}$, the port side experiences more concentrated pressure, with the high-pressure region progressively moving to the starboard side as r' increases. A gradual increase in pressure on the starboard bow leads to the emergence of negative pressure on both the port side and the starboard side at the stern.

Figures 15–17 display the forces and moments on the hull measured and fitted during the oblique towing test and circular motion test. It is observed that all three parameters tend to increase as the drift angle rises. Within the drift angle range specified by the oblique towing test, the lateral force and the yaw moment demonstrate an approximate linear response. However, the longitudinal force shows minimal sensitivity to drift angle variations. When $\beta = 0^{\circ}$, the longitudinal force acting on the hull can be represented by $X = X(u)$. Similarly, at smaller β values, the longitudinal force on the hull remains essentially constant. As the drift angle β increases, the lateral force correspondingly rises, with its rate of increase accelerating alongside β. In circular motion tests, changes in drift angle and the yaw velocity significantly influence both the lateral force and the yaw moment. When $\beta = 0^{\circ}$, the behavior of longitudinal force mirrors that observed in the oblique towing test. However, the lateral force and yaw moment exhibit heightened sensitivity to variations in the yaw velocity. As yaw velocity increases, the lateral force on the hull progressively rises, with each increment being larger than the last. Meanwhile, the yaw moment diminishes, with its overall magnitude slightly decreasing.

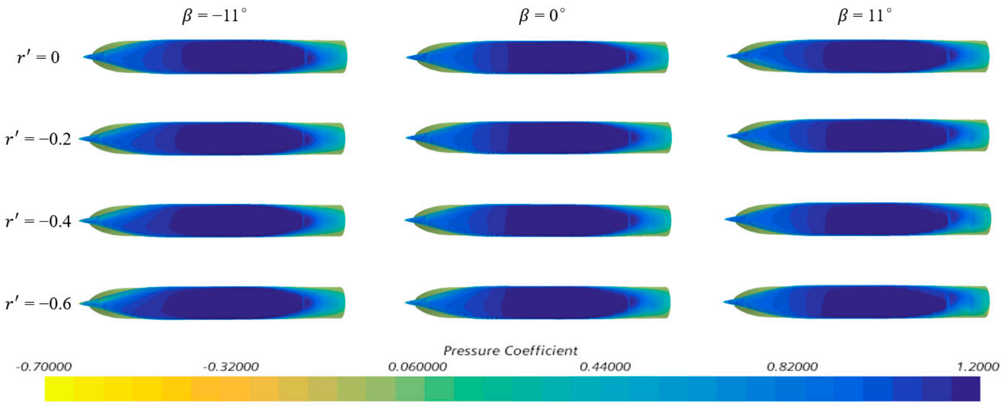

Figure 14. Hull's bottom pressure distribution in varies test conditions.

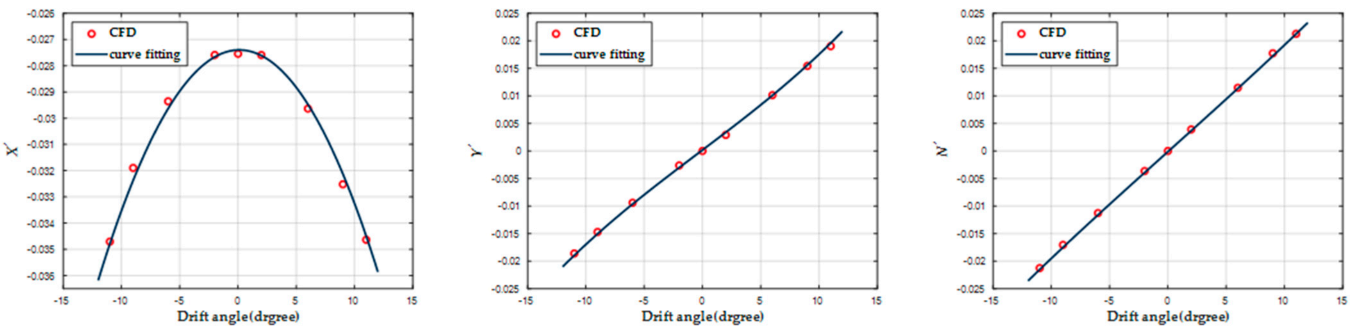

(**a**) (**b**) (**c**)

Figure 15. Simulation results of OTT: (**a**) longitudinal force; (**b**) lateral force; (**c**) yaw moment.

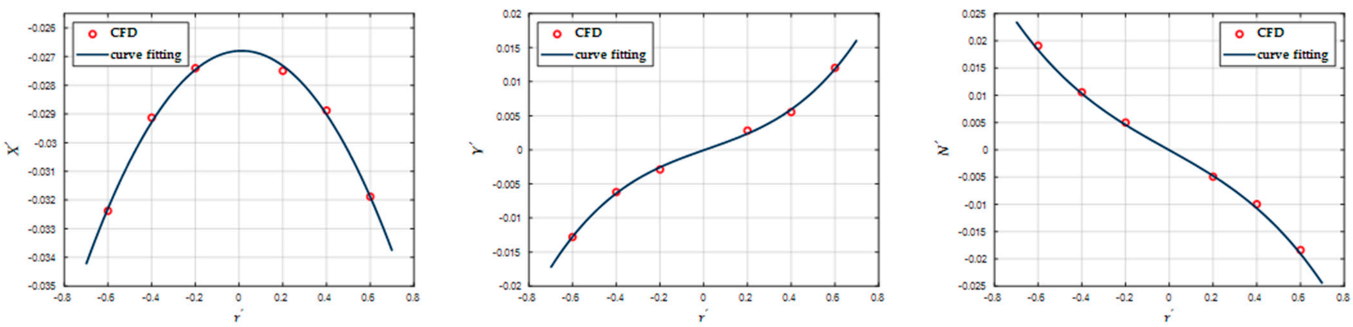

(**a**) (**b**) (**c**)

Figure 16. Simulation results of CMT (when $\beta = 0^\circ$): (**a**) longitudinal force; (**b**) lateral force; (**c**) yaw moment.

Through simulations at varying yaw velocities, it is observed that lower yaw velocity results in smoother transitions in the three curves, indicating a lesser impact from drift angle actions. Additionally, at drift angle $\beta > 0^\circ$, the longitudinal force on the hull attains a minimum value at some point.

A least squares regression analysis of the simulation outcomes yielded the hydrodynamic derivatives presented in Table 5. The empirical formulas are obtained from reference [27,30] and enable direct calculation of the hydrodynamic derivatives from parameters such as the ship length and breadth. When these results are compared to empirical formulas, some discrepancies are shown in the CFD findings. The calculated values of the linear hydrodynamic derivatives align with those from empirical formulas, maintaining a similar order of magnitude. However, greater differences are observed in some nonlinear hydrodynamic derivatives, potentially because the numerical simulations fail to precisely forecast hydrodynamic forces at higher drift angles. Furthermore, all lateral hydrodynamic derivatives appear to be underestimated, potentially because of challenging flow separations occurring at the hull's curvature under conditions of significant drift angles and high bow angular velocities.

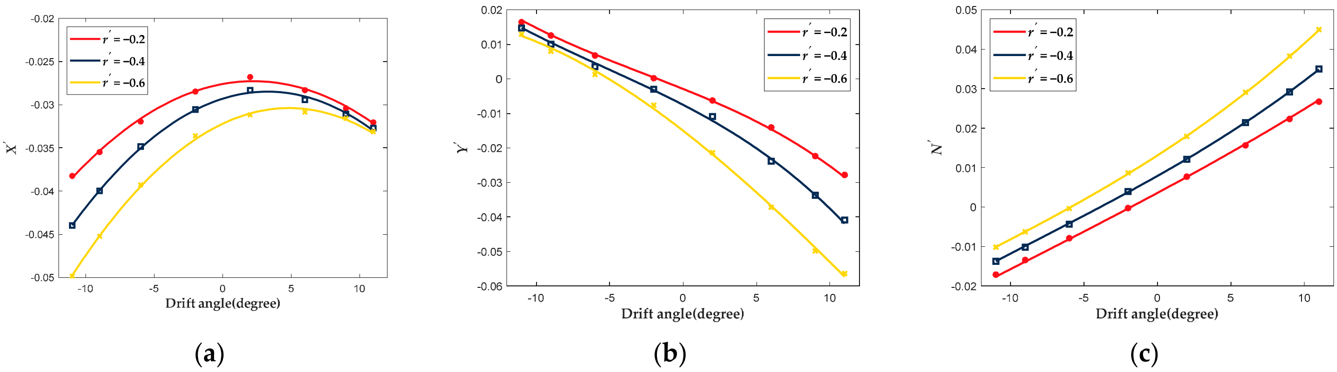

Figure 17. Simulation results of CMT (when r' = −0.2~−0.6): (**a**) longitudinal force; (**b**) lateral force; (**c**) yaw moment.

Table 5. Results of hydrodynamic derivative calculations and comparisons.

Hydrodynamic Derivative	CFD	Empirical Formula	Difference (%)	Hydrodynamic Derivative	CFD	Empirical Formula	Difference (%)
X_{uu}	−0.1015	−0.0837	21.29	Y_{vvr}	0.05243	0.0405	29.46
X_{vv}	−0.0474	−0.1391	65.91	Y_{vrr}	1.0639	0.2341	554.46
X_{vr}	−0.0019	−0.0007	164.15	N_v	−0.0784	−0.0467	67.88
X_{rr}	0.0780	0.1010	22.77	N_r	−0.0184	−0.0331	44.41
Y_v	−0.1295	−0.3082	57.98	N_{vv}	−0.0161	−0.0114	41.23
Y_r	0.0072	−0.1633	104.42	N_{rr}	−0.0209	−0.0227	7.92
Y_{vv}	−0.5809	−2.0374	71.49	N_{vvr}	−0.1012	−0.1845	45.15
Y_{rr}	−0.0219	−0.0080	174.24	N_{vrr}	0.0840	0.0257	226.85

Overall, the hydrodynamic derivatives derived from CFD calculations show acceptable differences from those calculated using empirical formulas, with large differences in some of the higher order and cross-coupled hydrodynamic derivatives.

4. Maneuverability Simulation and Verification

Utilizing the four-degree-of-freedom MMG equations for a fully rotary propelled ship, this study calculates hydrodynamic derivatives through empirical formulae and CFD simulations. Subsequently, time-domain differential equations are solved to facilitate computer simulations of the ship maneuvering dynamics, enabling the determination of its motion trajectory and maneuvering characteristics. The study conducts numerical simulations of the ship's 10° turning motion and ±10° zigzag motion under the assumption that both left and right propellers maintain constant rotational speeds and receive identical motion commands throughout the simulation process.

Concurrently, a full-scale trial is conducted in calm waters using the same commands, allowing for a direct comparison between the simulated tests and actual ship performance, as depicted in Figure 18. Additionally, a comparison of characteristic parameters for the turning and zigzag motions is presented in Tables 6 and 7.

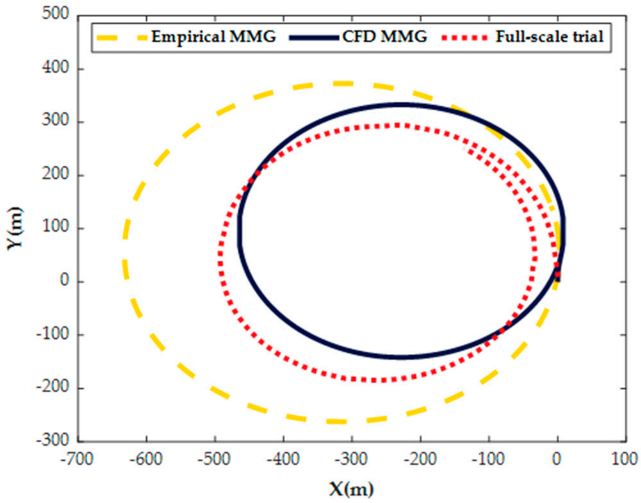

(**a**)

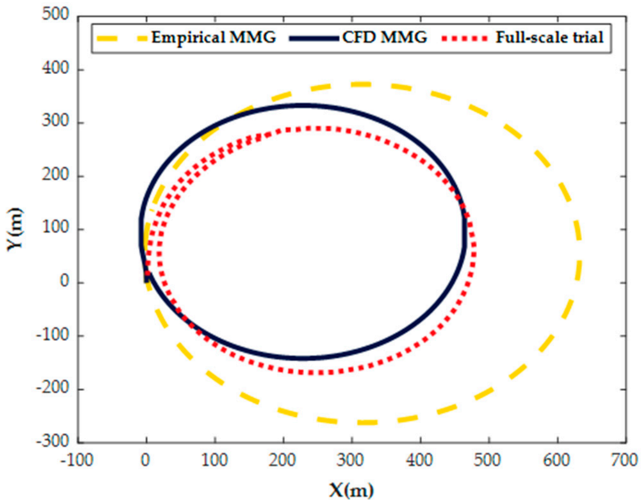

(**b**)

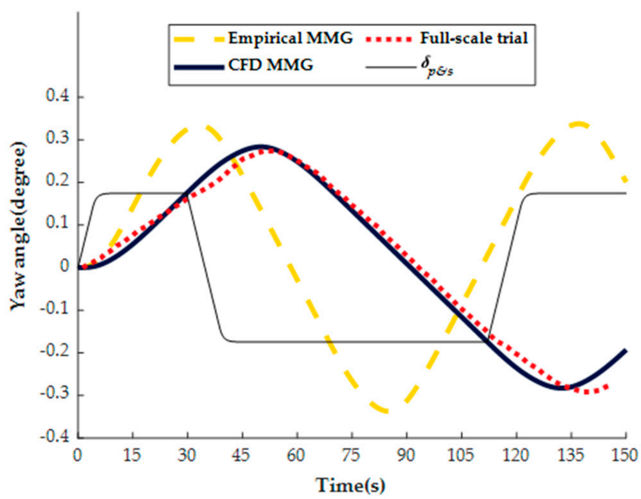

(**c**)

Figure 18. Simulation and test curves: (**a**) left turning at 10°; (**b**) right turning at 10°; (**c**) Zigzag test motion at ±10°.

Table 6. Comparison of characteristic parameters of turning test.

Main Parameters	Test Case	Full-Scale Trial	Empirical MMG	Error (%)	CFD MMG	Error (%)
Tactical Diameter (m)	Left turning at 10°	487.1	632.26	29.80	465.59	4.42
	Right turning at 10°	474.5	629.56	32.68	464.54	2.10
Advance (m)	Left turning at 10°	289.8	372.42	28.51	332.89	14.87
	Right turning at 10°	287.2	372.54	29.71	332.75	15.86
Transfer (m)	Left turning at 10°	195.9	329.03	67.96	220.98	12.80
	Right turning at 10°	205.8	323.69	57.28	217.19	5.53
Stabilized rolling angle (deg)	Left turning at 10°	1.99	1.64	18.00	1.72	13.57
	Right turning at 10°	1.98	1.66	17.01	1.71	13.64

Table 7. Comparison of characteristic parameters of zigzag test.

Main Parameters	Test Case	Full-Scale Trial	Empirical MMG	Error (%)	CFD MMG	Error (%)
1st overshoot (deg)	Zigzag test at ±10°	6.20	9.16	47.74	6.28	1.03
2nd overshoot (deg)		7.00	9.44	34.85	6.42	8.28

The graphical data illustrates that the ship's maneuvering parameters simulated during the CFD MMG tests align with the parameters observed in the full-scale trial. Furthermore, the ship's turning capabilities and directional stability meet the IMO's standards for maneuverability. The simulation accurately reproduced the tactical diameters observed during the turning motion to within a 5% error of the real ship test data. Nevertheless, the overall motion trajectory deviates slightly from the full-scale trial, which is caused by the interference of wind and wave factors present in the full-scale test, leading to a lateral shift in the ship's trajectory. While the current simulation only considers calm water conditions, as a result, the simulation errors for both advance and transfer are significantly larger and add to the uncertainty of rolling angle simulation; however, the transfer error is reduced when sailing upwind in the right turning at 10°. The error for the overall parameter characteristics is kept within 15%, which is an acceptable threshold, although there are also errors arising from scale effects inherent in the simulation. The CFD MMG method exhibits higher accuracy compared to the empirical MMG model.

During the zigzag maneuvering motion test, the simulated yaw direction and test curve largely align, exhibiting minimal error in the first overshoot angle. However, as calculation iterations progress, the cumulative time error incrementally escalates. Nevertheless, the overall deviation of the zigzag maneuvering motion parameters derived from the simulation remains below 10%, closely mirroring the full-scale trial data.

The methodology employed in this study markedly diminishes simulation errors across all maneuvering motion characteristic parameters compared to empirical MMG method. It can calculate more accurate hydrodynamic parameters in advance and obtain the ship's motion response through a rapid mathematical model calculation, and so its computational cost is significantly reduced compared with the CFD direct simulation method and experiments. This enhances the precision of maneuverability predictions at an acceptable computational expense, rendering it highly conducive to validating and optimizing ship maneuverability during the design phase.

5. Conclusions

This study offers a comprehensive prediction of the "Zhifei" ship's maneuvering motion, utilizing CFD technology and empirical formulas. This approach presents a viable method for accurately and rapidly forecasting maneuvering performance at the design stage of contemporary ships. Initially, the study conducts CFD numerical simulations on the captive motion model of "Zhifei", deriving all necessary hydrodynamic derivatives for the ship's maneuvering through both regression analysis and empirical formulas. Subsequently, based on the MMG mathematical model, a maneuvering motion mathematical model suitable for dual full-rotary propulsion ships is formulated. The model's turning and zigzag maneuvering motions is then numerically simulated. Finally, a full-scale trial maneuverability test is conducted, and the data from this test is compared and analyzed alongside the simulation outcomes, leading to the following key conclusions:

(1) The RANS-based numerical simulation method effectively predicts the hydrodynamic characteristics of the "Zhifei" hull. The hydrodynamic curves derived from the captive model tests align with the ship's behavior trend. However, there is a notable deviation in the hydrodynamic characteristics obtained post-regression analysis when compared to empirical formulas.
(2) This study introduces a four-degree-of-freedom maneuverability prediction technique for dual full-rotary propulsion ships. It evaluates the turning and zigzag maneuvering motion simulation results—derived from empirical formulas and CFD simulations—against full-scale trial test data, validating the mathematical model's efficacy for dual full-rotary propulsion ships. The results show that all maneuverability parameters have an error of less than 15% from the full-scale trial data. The error of the tactical diameter in the turning test is less than 5%, and the rest of the parameters may be affected by the wind and waves with an error of about 10%. The errors in the zigzag test are all within 10%.
(3) Currently, the research presented in this paper is limited to the four-degree-of-freedom maneuvering motion of ships in calm water. However, in real-world conditions, the interaction of wind, waves, currents and other environmental factors introduces some degree of error in the comparative results. Consequently, incorporating these factors into ship maneuvering studies represents the next focal point of future work.

Author Contributions: Conceptualization, Y.Y. and Q.Y.; methodology, Y.Y. and Y.T.; software, Y.Y., X.G. and Y.L.; validation, Y.T., Y.L. and X.G.; formal analysis, X.G. and Y.L.; investigation, X.G. and Y.L.; resources, Y.T., Y.L. and Y.J.; data curation, Q.Y. and Y.Y.; writing—original draft preparation, Y.Y. and Y.T.; writing—review and editing, Y.Y. and Y.J.; visualization, Y.T., Q.Y. and Y.J.; supervision, Q.Y. and Y.J.; project administration, Q.Y. and Y.J.; funding acquisition, X.G., Q.Y. and Y.J. All authors have read and agreed to the published version of the manuscript.

Funding: This research was funded by National Key Research and Development Program of China, grant number 2022YFB4301401.

Institutional Review Board Statement: Not applicable.

Informed Consent Statement: Informed consent was obtained from all subjects involved in the study.

Data Availability Statement: Data are contained within the article.

Conflicts of Interest: Author Yuhan Jiang was employed by the company Intelligent Navigation (Qingdao) Technology Co., Ltd. The remaining authors declare that the research was conducted in the absence of any commercial or financial relationships that could be construed as a potential conflict of interest.

Nomenclature

φ	roll angle	m_x	additional masses of the hull in the x axis
θ	pitch angle	m_y	additional masses of the hull in the y axis
ψ	yaw angle	X_{H}	hydrodynamic forces (moments)
u	surge velocity	X_{P}	longitudinal thrust force
v	sway velocity	Y_{P}	lateral thrust force
r	yaw velocity	K_{P}	rolling moment by propeller
m	hull mass	N_{P}	yawing moment by propeller
T	propeller thrust	I_{zz}	moment of inertia of the hull mass around the z axis
D	diameter of the propeller disk	J_{zz}	moment of additional inertia of the hull mass around the z axis

ρ	density of water	I_{xx}	moment of inertia of the hull mass around the x axis
n	rotation speed of propellers	J_{xx}	moment of additional inertia of the hull mass around the x axis
J	propeller advanced ratio	z_H	z axis coordinate of the point where Y_{H} acts
δ	rotation angle of propellers	L_{op}	longitudinal distance between propellers and ship's center of gravity
β	drift angle	L_{ps}	lateral distance between propellers
B	breadth	t_p	thrust deduction coefficient
λ	scale factor	ω_p	wake fraction at propeller position.
d	draft	R_G	convergence parameter
Δ	displacement	C_{b}	block coefficient
Z	number of blades	D_T	tactical diameter
Fr	Froude number	$X(u)$	resistance of the hull during straight sailing
		L_{pp}	length between perpendiculars
		L_{oa}	length overall

References

1. The Maneuvering Committee Final Report and Recommendations to the 24th ITTC. *Res. Propos.* **2005**, *1*, 137–140.
2. Yu, L.W.; Wang, S.Q.; Ma, N. Study on wave-induced motions of a turning ship in regular and long-crest irregular waves. *Ocean Eng.* **2021**, *195*, 108807. [CrossRef]
3. Abkowitz, M.A.; Liu, G. Measurement of ship resistance, powering and manoeuvring coefficients from simple trials during a regular voyage. *Soc. Nav. Archit. Mar. Eng.* **1988**, *96*, 97–128.
4. Ogawa, A.; Koyama, T.; Kijima, K. MMG report-I, on the mathematical model of ship manoeuvring. *Bull. Soc. Nav. Archit.* **1977**, *575*, 22–28.
5. Meng, Y.; Zhang, X.F.; Zhu, J.X. Parameter identification of ship motion mathematical model based on full-scale trial data. *Int. J. Nav. Archit. Ocean Eng.* **2022**, *14*, 100437. [CrossRef]
6. Fossen, T.I. A survey on Nonlinear Ship Control: From Theory to Practice. *IFAC Proc.* **2000**, *33*, 1–16. [CrossRef]
7. Sviličić, Š.; Rudan, S. Modelling Manoeuvrability in the Context of Ship Collision Analysis Using Non-Linear FEM. *J. Mar. Sci. Eng.* **2023**, *11*, 497. [CrossRef]
8. Shin, Y.J.; Kim, M.C.; Lee, K.W.; Jin, W.S.; Kim, J.W. Maneuverability Performance of a KRISO Container Ship (KCS) with a Bulb-Type Wavy Twisted Rudder and Asymmetric Pre-Swirl Stator. *J. Mar. Sci. Eng.* **2023**, *11*, 2011. [CrossRef]
9. Maciej, R. Prediction of manoeuvring abilities of 10,000 DWT pod-driven coastal tanker. *Ocean Eng.* **2017**, *136*, 201–208.
10. Sun, H.W.; Yang, J.L.; Liu, B.; Li, H.W.; Xiao, J.F.; Sun, H.B. Research on Maneuverability Prediction of Double Waterjet Propulsion High Speed Planing Craft. *J. Mar. Sci. Eng.* **2022**, *10*, 1978. [CrossRef]
11. Hajivand, A.; Mousavizadegan, S.H. Virtual simulation of maneuvering captive tests for a surface vessel. *Int. J. Nav. Archit. Ocean Eng.* **2015**, *7*, 848–872. [CrossRef]
12. Shenoi, R.R.; Krishnankutty, P.; Selvam, R.P. Study of manoeuvrability of container ship by static and dynamic simulations using a RANSE-based solver. *Ships Offshore Struct.* **2014**, *11*, 3:316–334. [CrossRef]
13. Li, S.L.; Liu, C.G.; Chu, X.M.; Zheng, M.; Wang, Z.P.; Kan, J.Y. Ship maneuverability modeling and numerical prediction using CFD with body force propeller. *Ocean Eng.* **2022**, *264*, 112454. [CrossRef]
14. Guo, H.P.; Zou, Z.J. System-based investigation on 4-DOF ship maneuvering with hydrodynamic derivatives determined by RANS simulation of captive model tests. *Appl. Ocean. Res.* **2017**, *68*, 11–25. [CrossRef]
15. Okuda, R.; Yasukawa, H.; Matsuda, A. Validation of maneuvering simulations for a KCS at different forward speeds using the 4-DOF MMG method. *Ocean Eng.* **2023**, *284*, 115174. [CrossRef]
16. Dash, A.K.; Chandran, P.P.; Khan, M.K.; Nagarajan, V.; Sha, O.P. Roll-induced bifurcation in ship maneuvering under model uncertainty. *J. Mar. Sci. Technol.* **2016**, *21*, 689–708. [CrossRef]
17. Shen, Z.R.; Wan, D.C.; Carrica, P.M. Dynamic overset grids in openfoam with application to KCS self-propulsion and maneuvering. *Ocean Eng.* **2015**, *108*, 287–306. [CrossRef]
18. Wang, J.H.; Zou, L.; Wan, D.C. CFD simulations of free running ship under course keeping control. *Ocean Eng.* **2017**, *141*, 450–464. [CrossRef]
19. Carrica, P.M.; Mofidi, A.; Eloot, K.; Delefortrie, G. Direct simulation and experimental study of zigzag maneuver of KCS in shallow water. *Ocean Eng.* **2016**, *112*, 117–133. [CrossRef]
20. Sanada, Y.; Park, S.; Kim, D.H.; Wang, Z.Y.; Stern, F.; Yasukawa, H. Experimental and computational study of hull–propeller–rudder interaction for steady turning circles. *Phys. Fluids* **2021**, *33*, 127117. [CrossRef]
21. Yasukawa, H.; Yoshimura, Y. Introduction of MMG standard method for ship maneuvering predictions. *J. Mar. Sci. Technol.* **2015**, *20*, 37–52. [CrossRef]
22. Gierusz, W. Simulation model of the LNG carrier with podded propulsion Part 1: Forces generated by pods. *Ocean Eng.* **2015**, *108*, 105–114. [CrossRef]

23. Turan, O.; Ayaz, Z.; Aksu, S.; Kanar, J.; Bednarek, A. Parametric rolling behaviour of azimuthing propulsion-driven ships. *Ocean Eng.* **2008**, *35*, 1339–1356. [CrossRef]
24. Neatby, H.C.; Thornhill, E. Turning and stopping of a ship with twin Z-drive thrusters. *Ocean Eng.* **2024**, *293*, 116641. [CrossRef]
25. Piaggio, B.; Sommariva, G.; Franceschi, A.; Villa, D.; Viviani, M. Twin-screw vessel manoeuvrability: The traditional twin-rudder configuration vs. pod-drives. *Ocean Eng.* **2023**, *271*, 113725. [CrossRef]
26. China Launches Autonomous Container Ship Zhi Fei. Available online: https://marineindustrynews.co.uk/china-launches-autonomous-container-ship-zhi-fei/#:~:text=China%20is%20reported%20to%20have%20put%20the%20world%E2%80%99s,and%20a%20normal%20operating%20speed%20of%208%20knots (accessed on 4 May 2022).
27. Kijima, K.; Katsuno, T.; Nakiri, Y.; Furukawa, Y. On the manoeuvring performance of a ship with the parameter of loading condition. In Proceedings of the Autumn Meeting of the Society of Naval Architects of Japan, 27–28 November 1990; pp. 141–148.
28. Kim, D.J.; Yun, K.; Yeo, D.J.; Kim, Y.G. Initial and steady turning characteristics of KCS in regular waves. *Appl. Ocean. Res.* **2020**, *105*, 102421. [CrossRef]
29. He, Y.Y.; Mou, J.M.; Chen, L.Y.; Zeng, Q.S.; Huang, Y.M.; Chen, P.F.; Zhang, S. Will sailing in formation reduce energy consumption? Numerical prediction of resistance for ships in different formation configurations. *Appl. Energy* **2022**, *312*, 118695. [CrossRef]
30. Grim, O.; Hachmann, D.; Hansen, H.-J.; Isensee, J.; Kastner, S.; Keil, H.; Laudan, J.; Lee, K.-Y.; Misra, P.N.; Ple, E.; et al. Ship structure loads and stresses. *Ocean Eng.* **1980**, *7*, 571–658. [CrossRef]